coatings

MDPI

*Article*

# Surface Modification of AM60 Mg-Al Alloy with Vanadium and $V_2O_5$ Sputtered Deposits: Activity in Marine Ambience

**Gerardo Sánchez, Lucien Veleva * and Eduardo Flores**

Applied Physics Department, Center for Research and Advanced Studies (CINVESTAV-Merida), Merida 97310, Mexico; gerardo.sanchezs@cinvestav.mx (G.S.); eduardo.flores@cinvestav.mx (E.F.)
* Correspondence: veleva@cinvestav.mx; Tel.: +52-999-9429477

**Abstract:** Vanadium (~450 nm) and $V_2O_5$ (~350 nm) were deposited by DC magnetron sputtering on an AM60 substrate to improve its degradation resistance in marine ambience. According to Raman and XPS analysis, the vanadium nanofilm mainly consists of amorphous $V_2O_3$, while $V_2O_5$ comprises two sheets of $VO_5$ and $VO_4$ units. After 30 days of immersion of the coated AM60 in a marine model solution (SME), the shift of the pH of the SME to more alkaline values was less pronounced for $V_2O_5$-AM60 because of the HCl acid formation during the partial dissolution of $V_2O_5$ in the presence of NaCl, and thus, a higher concentration of $Mg^{2+}$ ions $\sim$ 100 mg $L^{-1}$ was released from the Mg (AM60) matrix. The lower concentration of $\sim$ 40 mg $L^{-1}$ from the V-AM60 surface was attributed to the possible intercalation of the released Mg ions (cations) into the conductive tunnels of $V_2O_3$ as the main component of the vanadium sputtered deposit. This oxide has been reported as a material for high-capacitive energy storage. In this way, the V-deposit provided longer partial protection for the AM60 surface (Mg matrix) from localized pitting attacks.

**Keywords:** vanadium; vanadium oxides; sputtered deposits; magnesium–aluminum alloy degradation; marine ambience



**Citation:** Sánchez, G.; Veleva, L.; Flores, E. Surface Modification of AM60 Mg-Al Alloy with Vanadium and $V_2O_5$ Sputtered Deposits: Activity in Marine Ambience. *Coatings* **2024**, *14*, 955. https://doi.org/10.3390/coatings14080955

Academic Editors: Juan Manuel Vazquez Martinez and Jorge Salguero

Received: 13 July 2024
Revised: 26 July 2024
Accepted: 29 July 2024
Published: 1 August 2024



## 1. Introduction

In recent years, the reduction in the weight of automobiles has become a key focus in the transport industry to decrease fuel consumption and harmful gas emissions [1]. Light alloys have gained significant attention in the transport manufacturing industries, and magnesium (Mg) and Mg-based alloys stand out as a particularly promising candidate due to their properties. The low density (1.74 g $cm^{-3}$) and high strength-to-weight ratio (490 kN $m^{-1}kg^{-1}$) offer tremendous potential for reducing the weight of vehicle structures, leading to improved energy efficiency and a reduced carbon footprint ratio [2]. In this aspect, Mg is a key player in the quest for sustainable and eco-friendly solutions, raising Mg-based alloys to the esteemed position of being the third most widely preferable metallic materials in the automotive sector and aircraft industries [3].

In addition to the remarkable mechanical properties, the inherent susceptibility of Mg-based alloys to corrosion presents an obstacle in aggressive environments, which contain metal-reactive species, such as $Cl^-$ ions and $SO_2$ and $CO_2$ gasses, that cause the severe electrochemical degradation of magnesium [4–6]. Two simultaneous reactions take place during this process: an anodic oxidation reaction of the metal, leading to the formation of an insoluble layer of $Mg(OH)_2$ on the Mg surface, and a cathodic reduction reaction with the evolution of $H_2$ gas [7]. However, in marine environments, the $Cl^-$ ions can penetrate the pores of the $Mg(OH)_2$ corrosion layer, and the highly soluble $MgCl_2$ product (56.0 g $L^{-1}$ in water) is formed, accompanied by the release of $Mg^{2+}$ ions and $OH^-$ ions (pH increase), indicating a more accelerated degradation process [8]. This hinders the extensive application of Mg alloys in high-volume vehicle production.

Numerous approaches have been utilized to prevent the corrosion through different types of surface treatment or the modification of Mg-Al alloys. For instance, the application

of a coating can provide the formation of a physical barrier between the environment and the metal surface [9,10].

Physical vapor deposition (PVD) techniques are widely employed for the coating deposition of thin films, improving the metal surface mechanical properties (wear resistance, scuffling resistance, and surface roughness), the optical properties of microelectronics sensors, and corrosion resistance [11–15]. During the PVD process, the target material is transformed into atomic particles, which are then directed toward the metal surface substrate within a vacuum environment or gaseous plasma under low-pressure conditions. Upon reaching the substrates, the atomic particles condense and deposit as a physical coating [16]. The following two PVD methods may lead the motion of particles to deposition: evaporation and sputtering [17–20]. During the magnetron sputtering (either DC or RF), the target material is eroded by energetic Ar ions, resulting in ejecting atomic-sized particles, which will be deposited on the metal substrate. In the DC reactive magnetron sputtering, the oxygen is injected into the chamber and mixed with the metal atoms eroded from the target surface, and then oxide metallic compounds are formed and deposited on the metal substrate.

Vanadium has demonstrated a notable corrosion resistance when exposed to a variety of environments, including substitute ocean water, 3% sodium chloride solution (NaCl), tap water, and organic salts [21–23]. A vanadium layer was deposited on a zinc substrate through immersion in a solution containing vanadate [24], a compound of the oxyanion of vanadium (in an oxidation state of +5). The corrosion test revealed that the zinc surface modified with the vanadium layer exhibited a substantial enhancement in corrosion resistance.

The composition of the vanadium protective layer primarily consists of $V_2O_5$, $VO_2$, $V_2O_5{\cdot}nH_2O$, and $VO(OH)_2$ hydrates. Vanadium pentoxide ($V_2O_5$) has garnered significIts ant attention in recent years due to its semiconducting and electrochemical characteristics, making it highly suitable for integration into various technological applications in optical technologies, photochromic and electrochromic devices, and color memory devices [25–28]. Thin films of $V_2O_3$, $VO_2$ and $V_2O_5$ have been deposited on a range of substrates via the following: encompassing electron beam evaporation (on glass); magnetron sputtering, pulsed laser, and chemical vapor deposition (on Si); spray pyrolysis (on $Pt/TiO_2/SiO_2/Si$); spin coating (on ITO glass); and electrodeposition (on carbon fiber cloth) [29–34]. Polypyrrole and $V_2O_5$ composite films, formed by nanowires of 50 nm, have been deposited on the Mg surface at room temperature and at normal atmospheric pressures [35] to improve the corrosion resistance of Mg in a 3.5% wt.% NaCl solution. The reported results suggested that such kinds of composites could protect and slow down the reactivity of the Mg surface.

In previous research [36,37], an extensive corrosion study was carried out to characterize the activity of AM Mg-Al alloys exposed to a simulated marine-coastal environment (SME). The results indicated that the surface of the AM60 alloy would benefit from subsequent treatment or the application of protective coatings to enhance the corrosion resistance in the presence of $Cl^-$ ions, being a mainly aggressive component of the marine environments. Building upon these insights, the present study seeks to further enhance the corrosion resistance of AM60, exploring the specific characteristics of metallic vanadium and $V_2O_5$ as sputtered deposits. The change in the time of the SME pH solution and the concentration of the released $Mg^{2+}$ ions were monitored for a 30-day period to correlate with the surface microstructural characteristics identified by scanning electron microscopy–energy dispersive spectroscopy (SEM-EDS), X-ray photoelectron spectroscopy (XPS), and Raman confocal spectrometry. The corrosion behavior of the bare AM60 and that coated with vanadium and $V_2O_5$ sputtered deposits were compared. To the best of our knowledge, this is the first investigation with this approach.

## 2. Materials and Methods

### *2.1. Samples of AM60 and SME Model Solution*

Samples of extruded AM60 cylindrical alloy rods (10 mm in diameter) were provided by the Magnesium Innovation Center (Bottrop, Germany), and, according to the manufacture specification, the composition (wt. %) is as follows: 6.0% Al, manganese (Mn) ranging from 0.2% to 0.4%, and the balance Mg. The AM60 disk samples were cut with a thickness of 1 mm, and their surface was polished with silicon carbide (SiC) sandpaper sheets with grit sizes spanning from 400 to 1000, sonicated in ethanol for 5 min, and air-dried at room temperature (21 °C). The marine-coastal model solution composition of SME [36] consisted of 5.84 g $L^{-1}$ NaCl, 4.09 g $L^{-1}Na_2SO_4$, and 0.20 g $L^{-1}$ $NaHCO_3$ Aldrich analytical-grade reagents, which were dissolved in ultrapure deionized water (18.2 MΩ). The measured pH of the solution was 7.80 (PH60 Premium Line, pH tester, Apera Instruments, LLC., Columbus, OH, USA).

### *2.2. Coating Deposition*

The deposition of thin films on the AM60 Mg-Al alloy surface was performed through two different techniques: DC magnetron sputtering to obtain various $V_xO_y$ phase films of vanadium deposit through air exposure (Figure 1a), and DC reactive magnetron sputtering for $V_2O_5$ deposition (Figure 1b). The vacuum chamber for both techniques achieved a base vacuum pressure of $1 \times 10^{-5}$ Torr. Argon (Ar) was employed to generate an Ar plasma, and a constant working pressure of 4 mTorr was maintained during the vanadium deposition. For the DC reactive magnetron sputtering, a gas mixture of $Ar/O_2$ (4:1) was used, maintaining a total pressure of 5 mTorr for the $V_2O_5$ film deposition. The deposits were obtained on the surface of the AM60 substrate at room temperature (RT). The $V_2O_5$-AM60 was subjected to a post-deposition heat treatment at 300°C for 1 h under ambient conditions. High purity V-target (99.5%) was used for both sputtering processes. To achieve a deposition rate of ∼ 10 nm $min^{-1}$, the power was set to 75 W and the working distance was maintained at 60 mm. The deposition was carried out under room temperature conditions, and the total deposition time was 25 min. It is suggested that the thin films produced by the sputtering technique may exhibit imperfections that affect the interaction between the electrolyte and the substrate [15].

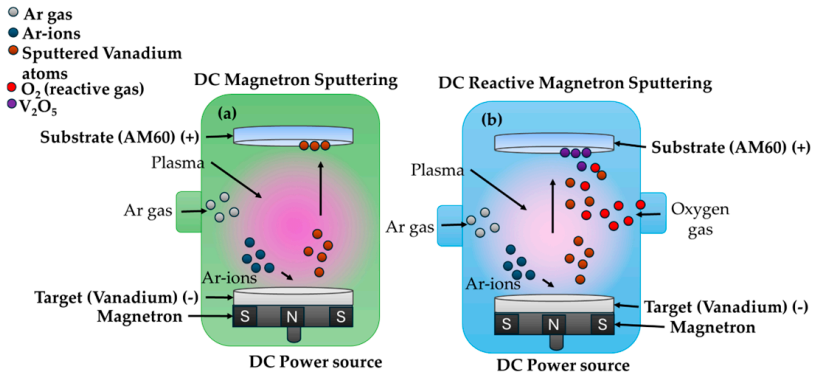


**Figure 1.** A schematic illustration of the (**a**) DC magnetron sputtering and (**b**) DC reactive magnetron sputtering deposition processes.

### *2.3. Immersion Test and Surface Characterization*

The AM60 samples, on the surfaces of which there were sputtered deposits of vanadium and $V_2O_5$, were submitted to immersion tests for 1, 7, 10, 15, and 30 days in 50 mL of SME, separately and triplicated, according to ASTM G31-12a [38]. Concluding the periods of time, the samples were washed and dried at room temperature (21 °C). The remaining solutions were used to measure the change in the time and pH of the SME solution and the concentration of Mg-released ions (HI83200, Hanna Instruments, Woonsocket, RI, USA).

The surface composition and morphology of the deposits on the AM60 substrate were evaluated by SEM-EDS (XL-30 ESEM-JEOL JSM-7600, IEOL Ltd. Tokyo, Japan). X-ray photoelectron spectroscopy (XPS, K-Alpha, Thermo-Scientific, Waltham, MA, USA) was implemented at different times of erosion with a scanning Ar ion gun, and it was conducted to provide additional information. The binding energies of the XPS spectra were normalized to a C1s emission peak of 284.8 eV. The Raman confocal spectrometer (Raman alpha300 WITech GmbH, Ulm, Germany) equipped with an argon ion laser was employed to identify vanadium thin films.

## 3. Results

### *3.1. Morphology of the Vanadium and $V_2O_5$ Deposits on AM60 Surface*

The SEM micrographs (Figure 2) compare the morphology of the bare AM60 surface (Figure 2a) with those of V-AM60 (Figure 2b) and $V_2O_5$-AM60 (Figure 2c). The EDS analysis of the bare AM60 (Table 1) suggested the presence of the Al-Mn intermetallic particles (Zone 1) and the $\beta$-$Mg_{17}Al_{12}$ secondary phase (Zone 2), which are characteristic of the Mg-Al alloy matrix (Zone 3). Meanwhile, the V-AM60 (Figure 2b) indicated the presence of singular particles of Al-Mn (Zone 4), in whose vicinity the vanadium nucleated; the content of V-deposit (Zones 4 and 5) was ~28 wt.%. In a similar way, Al-Mn particles were also found on the $V_2O_5$ deposit surface (Zone 6, SEM Figure 2c), and EDS analysis (Table 1) suggested vanadium ~15 wt.% (Zone 6) and a lower content of ~13 wt.% in Zone 7. Thus, it was considered that the Al-Mn particles, characteristic of the Mg-Al alloys, may partially disturb the formation of homogeneous V-deposits.

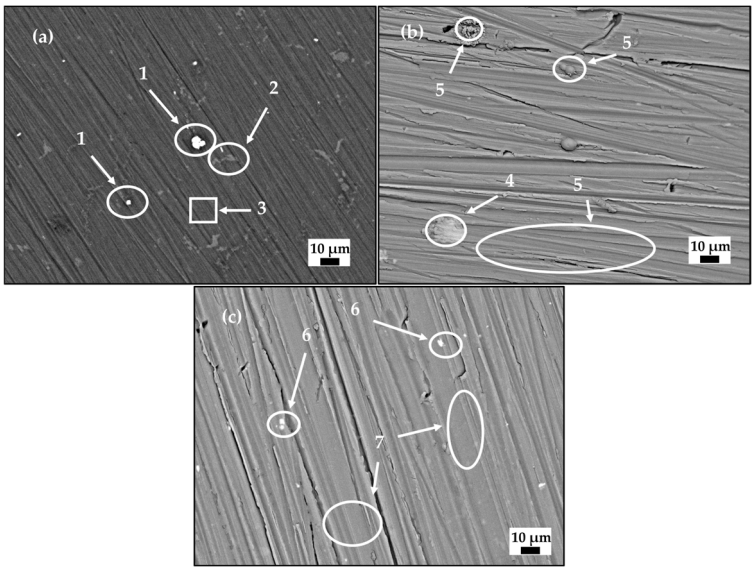


**Figure 2.** SEM micrographs of (**a**) bare AM60, (**b**) V-AM60, (**c**) $V_2O_5$-AM60.

**Table 1.** EDS elemental analysis (wt. %) of random selected surface areas (Figure 2) of the AM60 surface, V-AM60, and $V_2O_5$-AM60.

| | Element | O | Mg | Al | V | Mn |
|---|---|---|---|---|---|---|
| AM60 | Zone 1 | 2.93 | 35.07 | 31.47 | - | 30.53 |
| | Zone 2 | 1.34 | 76.95 | 21.71 | - | - |
| | Zone 3 | 2.12 | 92.50 | 5.38 | - | - |
| Vanadium | Zone 4 | 21.84 | 2.50 | 19.24 | 28.59 | 27.83 |
| | Zone 5 | 10.58 | 59.81 | 4.20 | 25.40 | - |
| $V_2O_5$ | Zone 6 | 12.99 | 33.14 | 23.27 | 15.32 | 15.28 |
| | Zone 7 | 13.42 | 60.78 | 12.70 | 13.10 | - |

The cross-sectional SEM images (Figure 3) helped to determine the thickness of the sputtered deposits on the AM60 substrate, considered ~400 nm for vanadium (Figure 3a,b) and ~320 nm for $V_2O_5$ (Figure 3c,d) nano-deposits.

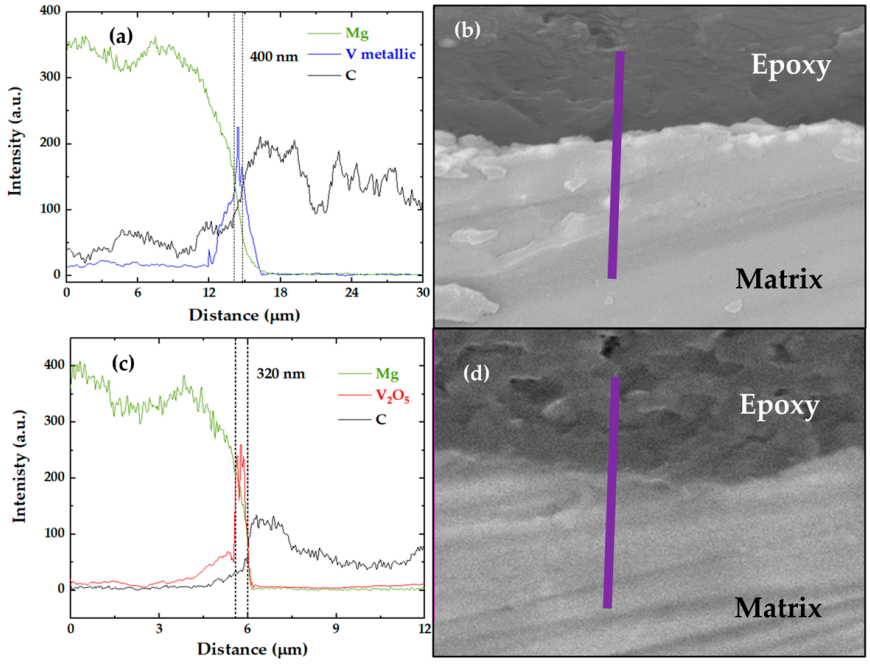


**Figure 3.** Cross-sectional SEM images (x5000) of (**a**,**b**) V-AM60 and (**c**,**d**) $V_2O_5$-AM60.

### *3.2. Raman Spectra and XPS Analysis of the Sputtered Deposits on AM60 Alloy Surface*

The Raman spectra of the vanadium (Figure 4a) and $V_2O_5$ (Figure 4b) nano-deposits were compared.

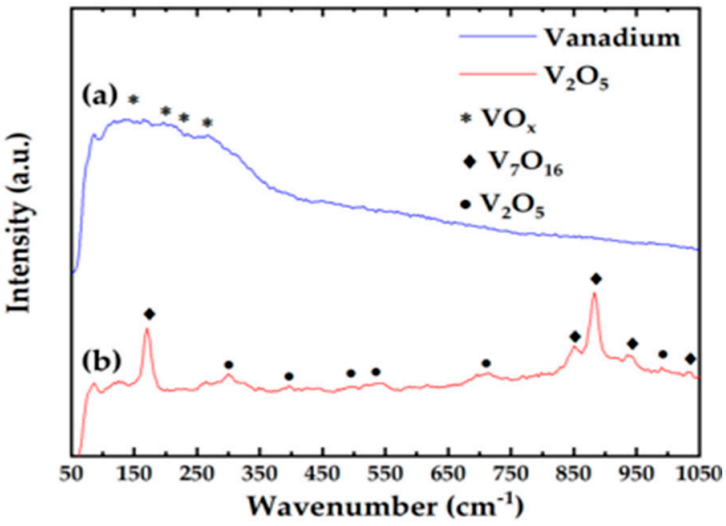


**Figure 4.** Raman spectroscopy of (**a**) vanadium and (**b**) $V_2O_5$ sputtered deposits on AM60 alloy surface.

According to study [39], there are approximately twenty stable $V_xO_y$ oxide phases, including VO, $V_2O_3$, $V_4O_7$, $V_6O_{11}$, $VO_2$, $V_6O_{13}$, $V_4O_9$, and $V_2O_5$. It was considered that vanadium film (Figure 4a) is composed of an amorphous mixture of $V_2O_3$ and a phase evolution to $VO_2$ [40,41], leading to the formation of thin films (with a thickness of nanometers). It has been suggested that the intensive peaks of V-O and V-V modes may appear in the range of 150–350 $cm^{-1}$ [42]; intensities are not well pronounced in the Raman spectrum

(Figure 4a). On the other hand, the spectrum of the $V_2O_5$ sputtered deposit on the AM60 surface alloy (Figure 4b) revealed peaks corresponding to $V_2O_5$ (marked with a circular shape) at 300, 398, 497, 537, 705, and 992 $cm^{-1}$, which were assigned to the vibrational modes of the $V_2O_5$ structure [39,43,44]. The low intensity peaks at 250–350 $cm^{-1}$ were ascribed to the bending vibrations of triply coordinated oxygen ($V_3-O$) of the $V_2O_5$ [45], as well as to the existence of doubly coordinated oxygen (V-O-V) [46]; the peak at ~990 $cm^{-1}$ was considered to belong to the terminal oxygen stretching mode due to unpaired electrons [39]. Moreover, the Raman spectrum (Figure 4b) presented the higher intensity peaks of $V_7O_{16}$, at 172, 851, 884, 941, and 1035 $cm^{-1}$, as characterized by two sheets, one comprising $VO_5$ units arranged in square pyramids and the other consisting of $VO_4$ units in tetrahedra. These sheets combine to form the layered structure of $V_7O_{16}$, which is similar to the reported signal for $V_2O_7$ and $V_3O_7$ [39,47,48].

To delve deeper into the structure of the sputtered deposits, an analysis of the XPS spectra (Figure 5) was performed. The distinct peaks of the V2p spectra were ascribed to different V-phases as a part of the sputtered deposit on the AM60 alloy surface.

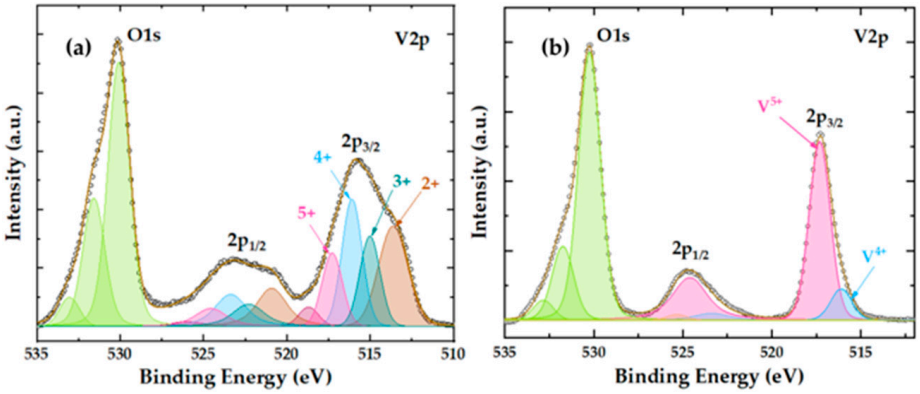


**Figure 5.** XPS V2p spectra of (**a**) vanadium and (**b**) $V_2O_5$ sputtered deposits on AM60 alloy surface.

The core level of the V2p spectrum of vanadium (Figure 5) exhibited two peaks of $V2p_{3/2}$ and $V2p_{1/2}$ ($\Delta$ = 7.3 eV), arising from spin-orbit splitting structures [49,50]. The deconvolution analysis of the $V2p_{3/2}$ energy level revealed the presence of four distinct peaks as follows: two peaks at ~517.28 eV and ~518.08 eV, representing $V^{5+}$ and $V^{4+}$ ions (FWHM of 1.43 eV for both signals) [49,51], and another two peaks at ~514.98 eV (1.43 eV FWHM) and ~513.58 eV (2.06 eV FWHM) [50,52,53], which may correspond to $V^{3+}$ and $V^{2+}$ ions, respectively. These peaks suggest that the sputtered vanadium oxidizes into $V_2O_3$ [53,54].

On the other hand, the analysis of the XPS spectra (Figure 5) provided the main peak of O1s at ~530.08 eV, which split into two additional peaks, presenting ~1.5 eV and ~3 eV higher binding energy, respectively. The O1s peaks were assigned to different oxides ($V_2O_3$ and $V_2O_5$), suggested by the Raman analysis (Figure 4), as a part of the sputtered deposits on the AM60 alloy surface. The XPS analysis of the sputtered $V_2O_5$ deposit (Figure 5b) indicated that the peaks of $2p_{1/2}$ and $2p_{3/2}$ are corresponding mainly to the high intensity of the $V^{5+}$ ion and the $V^{4+}$ ion at a lower intensity. Thus, the analysis of the XPS spectra provided a valuable tool for discerning the valence state of vanadium oxide structures.

### *3.3. Analysis of V-AM60 and $V_2O_5$-AM60 after Immersion in SME Marine Model Solution*

Figure 6a compares the gradual change of the initial pH=7.8 of the SME model solution during the 30 days of immersion of the AM60 alloy surface coated with vanadium and $V_2O_5$ sputtered deposits. The shift of pH overtime to more alkaline values (reaction 1) was less pronounced for the $V_2O_5$ deposit than that of vanadium on the AM60 surface, which may be attributed to the formation of HCl acid (reaction 2) during the dissolution of the $V_2O_5$ in aqueous solution in the presence of NaCl [55]. Since the thin nano-film

of $V_2O_5$ is gradually dissolving, the surface of the Mg (AM60) matrix is more exposed to deterioration and, as an indication, had a higher concentration of $Mg^{2+}$ ion release at ~100 mg $L^{-1}$ (Figure 6b) at 30 days (reaction 3) than that of ~ 40 mg $L^{-1}$ from the V-AM60 surface (Figure 6b).

$$Mg(OH)_2 + 2Cl^- \rightarrow MgCl_2 + 2OH^- \quad (1)$$

$$2NaCl + V_2O_5 + H_2O \rightarrow 2NaVO_3 + 2HCl \quad (2)$$

$$MgCl_2 \rightarrow Mg^{2+} + 2Cl^- \quad (3)$$

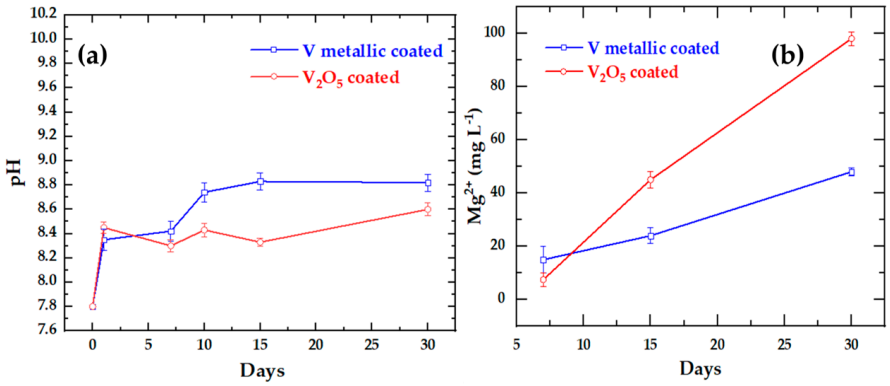


**Figure 6.** Change in time of SME marine solution: (**a**) pH and (**b**) concentration of $Mg^{2+}$ released ions during the immersion of V-AM60 and $V_2O_5$-AM60 for 30 days.

The SEM images (Figure 7) compare the morphology of the AM60 alloy surface coated with vanadium (Figure 7a) and $V_2O_5$ (Figure 7b) sputtered deposits after 30 days of immersion in the SME model solution. The emergence of microcracks observed can be attributed to the pressure exerted by $H_2$ bubbles (reaction 4) and likewise to the test sample removal from the solution and the subsequent air drying of the corrosion layer of $Mg(OH)_2$, which may undergo contraction due to its dehydration, thus forming microcracks in the surface film [56].

$$Mg^{2+} + 2H_2O \rightarrow Mg(OH)_2 + H_2 \quad (4)$$

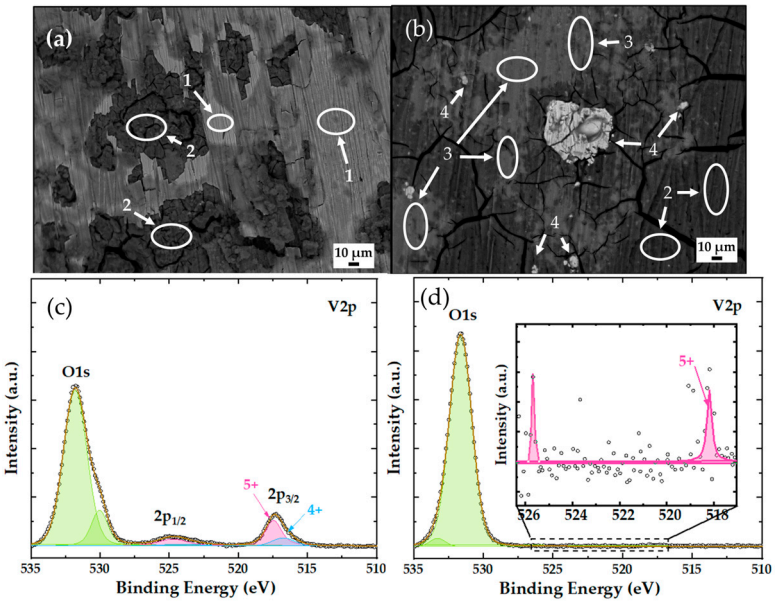


**Figure 7.** SEM images (x1000-LABE) of (**a**) V-AM60 and (**b**) $V_2O_5$-AM60. XPS spectra of (**c**) V-AM60 and (**d**) $V_2O_5$-AM60.

The EDS analysis (Table 2) of zones of interest on the V-AM60 surface (Figure 7a) indicated the presence of vanadium ~ 21.81 wt.% (Zone 1) and MgO ($Mg(OH)_2$, Zone 2) after 30 days of immersion in the SME solution. Meanwhile, on the $V_2O_5$-AM60 surface (Figure 7b), the vanadium content was very low at ~ 6.63 wt.% and was in separated zones (Zone 3), confirming the dissolution process of vanadium (reaction 2). Since the AM60 matrix has lost the deposit of $V_2O_5$, the multiple intermetallic particles of Al-Mn appeared (Zone 4), as is characteristic of AM60 (Figure 2), which remained unaffected by the corrosion process due their local cathodic activity, thus accelerating the cathodic reaction of $H_2$ and Mg matrix degradation (reaction 4).

**Table 2.** EDS elemental analysis (wt. %) of random selected surface areas (Figure 7) of V-AM60 and $V_2O_5$-AM60.

| | Element | O | Mg | Al | V | Mn |
|---|---|---|---|---|---|---|
| Vanadium | Zone 1 | 36.72 | 11.59 | 3.63 | 21.81 | - |
| | Zone 2 | 21.72 | 68.53 | 5.67 | - | - |
| $V_2O_5$ | Zone 3 | 11.28 | 66.32 | 14.77 | 6.63 | - |
| | Zone 4 | 31.01 | 14.73 | 17.47 | 0.22 | 35.84 |

To collaborate with the SEM-EDS, XPS analysis was carried out (Figure 7c,d). The XPS V2p analysis confirmed the presence of $V^{5+}$ and $V^{4+}$ ion signals as a part of the vanadium sputtered deposit (Figure 7c), while the sputtered $V_2O_5$ deposits (Figure 7d) showed signals of binding energy at a very low level, confirming $V_2O_5$ dissolution (reaction 2) during the 30 days of immersion in the SME solution because of the presence of NaCl ions.

Figure 8 compares the depths of localized corrosion attacks in the bare AM60 alloy (Figure 8a), vanadium (Figure 8b), and $V_2O_5$ (Figure 8c) sputtered deposits on the AM60 surface after immersion for 30 days in the SME model solution. The maximum value of ~154.50 µm was observed for V-AM60, whose surface gradually lost the V-deposit (reaction 2), while the $V_2O_5$-AM60 system presented a lower depth of ~ 32 µm and a maximum of 56.06 µm. Conversely, in the absence of sputtered deposits, the bare AM60 (Figure 8a) revealed a greater depth of ~90.18 µm. This comparative analysis highlights a reduction in localized corrosion attacks by ~Δ34.12 µm due to the partial protective effect of the $V_2O_5$ sputtered deposit.

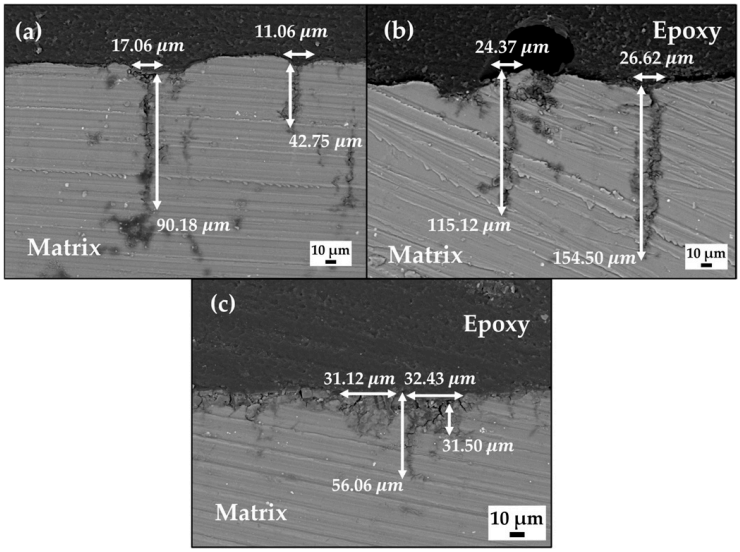


**Figure 8.** SEM images of the cross-sections of (**a**) bare AM60 alloy surface (x500), (**b**) V-coated (x370), and (**c**) $V_2O_5$-coated (x500).

A recent review [57] presents the introduction of vanadium-based compounds as prospective cathodes for Mg-Al-Zn alloys, proposed as materials for aqueous zinc ions batteries (AZIBs). The variety of vanadium oxide states, presenting different crystal structures and diverse coordination, have provided paths for $Zn^{2+}$ intercalation (storage) [58–62]. In our study, the presence of $V_2O_3$ was suggested by XPS analysis as a part of the vanadium sputtered deposit (Figure 5a), and it was considered that this oxide may present high-capacitive energy storage, having a structure like a conductive tunnel in which metal cations may be intercalated [63]. On the other hand, the Mg–Vanadium spinel oxide has been reported to have a higher capacitive for Mg ion storage in batteries (MIBs) [64].

We would like to consider that the released Mg ions from the Mg-Al alloy (AM60), observed in our study (Figure 6b) can be intercalated into the $V_2O_3$ conductive tunnels and stored there until saturation, followed by a stage of Mg ion gradual release over time. This fact will diminish the rate of $MgCl_2$ dissolution (reaction 3), and thus the vanadium sputtered deposit will provide a longer service life for the AM60 alloy surface during exposure to marine ambience.

## 4. Conclusions

Vanadium and $V_2O_5$ were deposited by DC magnetron sputtering on an AM60 substrate (Mg-Al alloy surface) to improve its corrosion resistance in marine ambience. The average thickness of the vanadium and $V_2O_5$ coatings was ~450 nm and ~350 nm, respectively. The presence of Al-Mn intermetallic isolated particles was found to be a part of the deposits, in whose vicinity the deposits nucleated. According to Raman and XPS analysis, the sputtered vanadium is mainly composed of amorphous $V_2O_3$, while the sputtered $V_2O_5$ comprises two sheets of $VO_5$ and $VO_4$ units.

Samples of V-AM60 and $V_2O_5$-AM60 were immersed for 30 days in a marine model solution (SME), where the initial pH (=7.8) shifted to more alkaline values, which were less pronounced for the $V_2O_5$ deposit than for that of vanadium on the AM60 surface, which can be attributed to the formation of HCl acid during the dissolution of $V_2O_5$ in the aqueous solution in the presence of NaCl. Therefore, the thin nano-deposit of $V_2O_5$ was gradually dissolved, and a higher concentration of $Mg^{2+}$ ions, $\sim 100$ mg $L^{-1}$, was released from the Mg (AM60) matrix when compared to that of $\sim 40$ mg $L^{-1}$ from the V-AM60 surface.

Considering $V_2O_3$ as the main component of the vanadium sputtered deposit, we would like to suggest the possible intercalation of the released Mg ions (cations) into the conductive tunnels of this oxide, reported as a material capable of high-capacitive energy storage. Thus, the V-deposit provided longer partial protection for the AM60 surface (Mg-matrix) from localized surface attacks (pitting).

The modification of the AM60 surface (Mg-Al-Mn alloy) is still a difficult problem to achieve for the improvement of the resistance in marine environments, largely since, in the Mg matrix, there are intermetallic particles and secondary phases (as active cathodes).

**Author Contributions:** G.S. performed the preparation of samples and the immersion tests; E.F. and G.S. contributed to the deposit sputtering methodology and post-deposition heat treatment of the vanadium and $V_2O_5$ coatings; G.S. and L.V. performed the formal analysis of the results and the writing of the original draft and its editing. L.V. supervised the project. All correspondence should be addressed to L.V. All authors have read and agreed to the published version of the manuscript.

**Funding:** This research received no external funding.

**Institutional Review Board Statement:** Not applicable.

**Informed Consent Statement:** Not applicable.

**Data Availability Statement:** The data are available upon request from the corresponding author.

**Acknowledgments:** Gerardo Sánchez acknowledges the Mexican National Council of Humanities, Science and Technologies (CONAHCYT) for the scholarship for his Ph.D. study. The authors gratefully thank the National Laboratory of Nano and Biomaterials (LANNBIO-CINVESTAV) for allowing the

use of SEM-EDS, XPS, and XRD facilities; thanks also go to Victor Rejón, Daniel Aguilar, and Willian Cauich for their support in data acquisition.

**Conflicts of Interest:** The authors declare no conflict of interest.

## References


1. Joost, W.J. Reducing Vehicle Weight and Improving U.S. Energy Efficiency Using Integrated Computational Materials Engineering. *JOM* **2012**, *64*, 1032–1038. [CrossRef]
2. Mordike, B.L.; Ebert, T. Magnesium Properties-Applications-Potential. *Mater. Sci. Eng. A* **2001**, *302*, 37–45. [CrossRef]
3. Powell, B.R.; Krajewski, P.E.; Luo, A.A. Magnesium Alloys for Lightweight Powertrains and Automotive Structures. In *Materials, Design and Manufacturing for Lightweight Vehicles*, 2nd ed.; Mallick, P.K., Ed.; Elsevier: Amsterdam, The Netherlands, 2020; pp. 125–186. [CrossRef]
4. Makar, G.L.; Kruger, J. Corrosion of Magnesium. *Int. Mater. Rev.* **1993**, *38*, 138–153. [CrossRef]
5. Altun, H.; Sen, S. Studies on the Influence of Chloride Ion Concentration and pH on the Corrosion and Electrochemical Behaviour of AZ63 Magnesium Alloy. *Mater. Des.* **2004**, *25*, 637–643. [CrossRef]
6. Kainer, K.U.; Srinivasan, P.B.; Blawert, C.; Dietzel, W. Corrosion of Magnesium and Its Alloys. In *Shreir's Corrosion—Corrosion and Degradation of Engineering Materials*; Cottis, B., Graham, M., Lindsay, R., Lyon, S., Richardson, T., Scantlebury, D., Stott, H., Eds.; Elsevier: Amsterdam, The Netherlands, 2010; Volume 3, pp. 2011–2041. [CrossRef]
7. Song, G.L.; Atrens, A. Corrosion Mechanisms of Magnesium Alloys. *Adv. Eng. Mater.* **1999**, *1*, 11–33. [CrossRef]
8. Haynes, W.M.; Lide, D.R.; Bruno, T.J. Section 5 Thermochemistry, Electrochemistry, and Solution Chemistry. In *CRC Handbook of Chemistry and Physics 97th Edition*, 97th ed.; Haynes, W.M., Lide, D.R., Bruno, T.J., Eds.; CRC Press: Boca Raton, FL, USA, 2017; pp. 167–173. [CrossRef]
9. Lunder, O. Corrosion Resistance of Cast Mg-Al Alloys. *Corros. Rev.* **1997**, *15*, 439–470. [CrossRef]
10. Hu, H.; Nie, X.; Ma, Y. Corrosion and Surface Treatment of Magnesium Alloys. In *Magnesium Alloys—Properties in Solid and Liquid States*; Czerwinski, F., Ed.; IntechOpen: London, UK, 2014; pp. 67–108. [CrossRef]
11. Mehran, Q.M.; Fazal, M.A.; Bushroa, A.R.; Rubaiee, S. A Critical Review on Physical Vapor Deposition Coatings Applied on Different Engine Components. *Crit. Rev. Solid State Mater. Sci.* **2018**, *43*, 158–175. [CrossRef]
12. Rossnagel, S.M. Directional and Ionized Physical Vapor Deposition for Microelectronics Applications. *J. Vac. Sci. Technol. B* **1998**, *16*, 2585. [CrossRef]
13. Altun, H.; Sen, S. The Effect of PVD Coatings on the Corrosion Behaviour of AZ91 Magnesium Alloy. *Mater. Des.* **2005**, *27*, 1174–1179. [CrossRef]
14. Mathew, M.T.; Ariza, E.; Rocha, L.A.; Fernandes, A.C.; Vaz, F. $TiC_xO_y$ Thin Films for Decorative Applications: Tribocorrosion Mechanisms and Synergism. *Tribol. Int.* **2008**, *41*, 603–615. [CrossRef]
15. Calderon, S.; Alves, C.F.A.; Manninen, N.K.; Cavaleiro, A.; Carvalho, S. Electrochemical Corrosion of Nano-Structured Magnetron-Sputtered Coatings. *Coatings* **2019**, *9*, 682. [CrossRef]
16. Moshfegh, A.Z. PVD Growth Methods: Physics and Technology. In Proceedings of the Physics and Technology of Thin films: IWTF 2003; Moshfegh, A.Z., Känel, H.V., Kashyap, S.C., Wuttig, M., Eds.; World Scientific: Singapore, 2004; pp. 28–53. [CrossRef]
17. Sproul, W.D. Physical Vapor Deposition Tool Coatings. *Surf. Coat. Technol.* **1996**, *81*, 1–7. [CrossRef]
18. Baptista, A.; Silva, F.J.G.; Porteiro, J.; Míguez, J.L.; Pinto, G.; Fernandes, L. On the Physical Vapour Deposition (PVD): Evolution of Magnetron Sputtering Processes for Industrial Applications. *Procedia Manuf.* **2018**, *17*, 746–757. [CrossRef]
19. Hoche, H.; Groß, S.; Oechsner, M. Development of New PVD Coatings for Magnesium Alloys with Improved Corrosion Properties. *Surf. Coat. Technol.* **2014**, *259*, 102–108. [CrossRef]
20. Petkoska, A.T.; Nasov, I. Surface Engineering of Polymers-Case Study: PVD Coatings on Polymers. *Zast. Mater.* **2014**, *55*, 3–10. [CrossRef]
21. Schlain, D.; Kenahan, C.B.; Acherman, W.L. Corrosion Properties of High-Purity Vanadium. *J. Less-Common Met.* **1961**, *3*, 458–467. [CrossRef]
22. Li, C.-W.; Tian, X.-B.; Liu, T.-W.; Qin, J.-W.; Gong, C.-Z. Microstructure and Corrosion Resistance of Vanadium Films Deposited at Different Target-Substrate Distance by HPPMS. *Rare Met.* **2014**, *33*, 587–593. [CrossRef]
23. Sun, R.; Yang, S.; Lv, T. Corrosion Behavior of AZ91D Magnesium Alloy with a Calcium–Phosphate–Vanadium Composite Conversion Coating. *Coatings* **2019**, *9*, 379. [CrossRef]
24. Zhongli, Z.; Ning, L.I.; Deyu, L.I. Corrosion Protection Properties of Vanadium Films Formed on Zinc Surfaces. *Rare Met.* **2011**, *30*, 146. [CrossRef]
25. Liu, J.; Wang, X.; Peng, Q.; Li, Y. Preparation and Gas Sensing Properties of Vanadium Oxide Nanobelts Coated with Semiconductor Oxides. *Sens. Actuators Chem. B* **2006**, *115*, 481–487. [CrossRef]
26. Cheng, K.C.; Chen, F.R.; Kai, J.J. $V_2O_5$ Nanowires as a Functional Material for Electrochromic Device. *Sol. Energy Mater. Solar Cells* **2006**, *90*, 1156–1165. [CrossRef]
27. Singhal, A.; Skandan, G.; Amatucci, G.; Badway, F.; Ye, N.; Manthiram, A.; Ye, H.; Xu, J.J. Nanostructured Electrodes for next Generation Rechargeable Electrochemical Devices. *J. Power Sources* **2004**, *129*, 38–44. [CrossRef]

28. Lukong, V.T.; Ukoba, K.; Jen, T.C. Fabrication of Vanadium Dioxide Thin Films and Application of Its Thermochromic and Photochromic Nature in Self-Cleaning: A Review. *Energy Environ.* **2023**, *34*, 3495–3528. [CrossRef]
29. Beke, S. A Review of the Growth of $V_2O_5$ Films from 1885 to 2010. *Thin Solid Films* **2011**, *519*, 1761–1771. [CrossRef]
30. Su, Q.; Lan, W.; Wang, Y.Y.; Liu, X.Q. Structural Characterization of $\beta$-$V_2O_5$ Films Prepared by DC Reactive Magnetron Sputtering. *Appl. Surf. Sci.* **2009**, *255*, 4177–4179. [CrossRef]
31. Hwang, K.S.; Kang, B.A.; Kim, S.D.; Hwangbo, S.; Kim, J.T. Amorphous Vanadium Pentoxide Thin Films Prepared by Electrostatic Spraying-Pyrolysis Deposition. *Ceram. Int.* **2011**, *38*, S645–S647. [CrossRef]
32. Mazur, M.; Lubańska, A.; Domaradzki, J.; Wojcieszak, D. Complex Research on Amorphous Vanadium Oxide Thin Films Deposited by Gas Impulse Magnetron Sputtering. *Appl. Sci.* **2022**, *12*, 8966. [CrossRef]
33. Diaz-Fernandez, Y.; Malavasi, L.; Quartarone, E. Flexible Deposition of Nanocrystalline Vanadium Oxide Thin Films. *J. Mater. Chem.* **2008**, *18*, 5190–5192. [CrossRef]
34. Velayutham, R.; Manikandan, R.; Raj, C.J.; Kale, A.M.; Kaya, C.; Palanisamy, K.; Kim, B.C. Electrodeposition of vanadium pentoxide on carbon fiber cloth as a binder-free electrode for high-performance asymmetric supercapacitor. *J. Alloys Compd.* **2021**, *863*, 158332. [CrossRef]
35. Li, J.; He, Y.; Sun, Y.; Zhang, X.; Shi, W.; Ge, D. Synthesis of Polypyrrole/$V_2O_5$ Composite Film on the Surface of Magnesium Using a Mild Vapor Phase Polymerization (VPP) Method for Corrosion Resistance. *Coatings* **2020**, *10*, 402. [CrossRef]
36. Chávez, L.; Veleva, L.; Sánchez, G.; Dieringa, H. AM60-AlN Nanocomposite and AM60 Alloy Corrosion Activity in Simulated Marine-Coastal Ambience. *Metals* **2022**, *12*, 1997. [CrossRef]
37. Chávez, L.; Veleva, L.; Sánchez-Ahumada, D.; Ramírez-Bon, R. Hybrid Coating of Polystyrene–$ZrO_2$ for Corrosion Protection of AM Magnesium Alloys. *Coatings* **2023**, *13*, 1059. [CrossRef]
38. *ASTM G31-12*; Standard Guide for Laboratory Immersion Corrosion Testing of Metals. ASTM International: West Conshohocken, PA, USA, 2021.
39. Shvets, P.; Dikaya, O.; Maksimova, K.; Goikhman, A. A Review of Raman Spectroscopy of Vanadium Oxides. *J. Raman Spectrosc.* **2019**, *50*, 1226–1244. [CrossRef]
40. Gauntt, B.D.; Li, J.; Cabarcos, O.M.; Basantani, H.A.; Venkatasubramanian, C.; Bharadwaja, S.S.N.; Podraza, N.J.; Jackson, T.N.; Allara, D.L.; Antrazi, S.; et al. Microstructure of Vanadium Oxide Used in Microbolometers. In *the Infrared Technology and Applications XXXVII., Proceedings of the SPIE, Orlando, FL, USA, 21 May 2011*; Volume 8012, p. 80123T. [CrossRef]
41. Petrov, G.I.; Yakovlev, V.V.; Squier, J. Raman Microscopy Analysis of Phase Transformation Mechanisms in Vanadium Dioxide. *Appl. Phys. Lett.* **2002**, *81*, 1023–1025. [CrossRef]
42. Marini, C.; Arcangeletti, E.; Castro, D.D.; Baldassare, L.; Perucchi, A.; Lupi, S.; Malavasi, L.; Boeri, L.; Pomjakushina, E.; Conder, K.; et al. Optical Properties of $V_{1-x}Cr_xO_2$ Compounds under High Pressure. *Phys. Rev. B* **2008**, *77*, 235111. [CrossRef]
43. Plugaru, R.; Mihalache, I.; Romaniţan, C.; Comanescu, F.; Vulpe, S.; Craciun, G.; Plugaru, N.; Djourelov, N. Light-Sensing Properties of Amorphous Vanadium Oxide Films Prepared by RF Sputtering. *Sensors* **2023**, *23*, 1759. [CrossRef] [PubMed]
44. Qing, S.; Xiajun, P.; Erqing, X.; Yinyue, W.; Jiawen, Q.; Xueqin, L. Influence of Temperature on the Microstructure of $V_2O_5$ Film Prepared by DC Magnetron Sputtering. *Rare Metals* **2006**, *25*, 82. [CrossRef]
45. Julien, C.; Nazri, G.A.; Bergström, O. Raman Scattering Studies of Microcrystalline $V_6O_{13}$. *Phys. Status Solid. B Basic Res.* **1997**, *201*, 319–326. [CrossRef]
46. Rana, A.; Rana, A.S. Investigation of $V_xO_y$ Thin Films Using Raman Spectroscopy: Role of Oxygen Vacancies and Structural Phase Transformation on Thermochromic Properties. *Mater. Today Proc.* **2023**. [CrossRef]
47. Huotari, J.; Lappalainen, J.; Eriksson, J.; Bjorklund, R.; Heinonen, E.; Miinalainen, I.; Puustinen, J.; Spetz, A.L. Synthesis of Nanostructured Solid-State Phases of $V_7O_{16}$ and $V_2O_5$ Compounds for Ppb-Level Detection of Ammonia. *J. Alloys Compd.* **2016**, *675*, 433–440. [CrossRef]
48. Hu, P.; Hu, P.; Vu, T.D.; Li, M.; Wang, S.; Ke, Y.; Zeng, X.; Mai, L.; Long, Y. Vanadium Oxide: Phase Diagrams, Structures, Synthesis, and Applications. *Chem. Rev.* **2023**, *123*, 4353–4415. [CrossRef] [PubMed]
49. Demeter, M.; Neumann, M.; Reichelt, W. Mixed-Valence Vanadium Oxides Studied by XPS. *Surf. Sci.* **2000**, *454*, 41–44. [CrossRef]
50. Mendialdua, J.; Casanova, R.; Barbaux, Y. XPS Studies of $V_2O_5$, $V_6O_{13}$, $VO_2$ and $V_2O_3$. *J. Electron Spectros. Relat. Phenom.* **1995**, *71*, 249–261. [CrossRef]
51. Silversmit, G.; Depla, D.; Poelman, H.; Marin, G.B.; De Gryse, R. Determination of the V2p XPS Binding Energies for Different Vanadium Oxidation States ($V^{5+}$ to $V^{0+}$). *J. Electron Spectros. Relat. Phenom.* **2004**, *135*, 167–175. [CrossRef]
52. Werfel, F.; Dräger, G.; Berg, U. X-Ray and X-Ray Photoelectron Spectra of Vanadium Oxides. *Cryst. Res. Technol.* **1981**, *16*, 119–126. [CrossRef]
53. Lindström, R.; Maurice, V.; Zanna, S.; Klein, L.; Groult, H.; Perrigaud, L.; Cohen, C.; Marcus, P. Thin Films of Vanadium Oxide Grown on Vanadium Metal: Oxidation Conditions to Produce $V_2O_5$ Films for Li-Intercalation Applications and Characterisation by XPS, AFM, RBS/NRA. *Surf. Interface Anal.* **2006**, *38*, 6–18. [CrossRef]
54. Sarma, D.D.; Rao, C.N.R. XPES Studies of Oxides of Second- and Third-Row Transition Metals Including Rare Earths. *J. Electron Spectros. Relat. Phenom.* **1980**, *20*, 25–45. [CrossRef]
55. Trypuc, M.; Kiełkowska, U.; Chałat, M. Articles Solubility Investigations in the NaCl + $V_2O5$ + $H_2O$ System from 293 K to 323 K. *J. Chem. Eng. Data* **2002**, *47*, 765–767. [CrossRef]

56. Song, Y.; Shan, D.; Chen, R.; Zhang, F.; Han, E.H. Biodegradable Behaviors of AZ31 Magnesium Alloy in Simulated Body Fluid. *Mater. Sci. Eng. C* **2009**, *29*, 1039–1045. [CrossRef]
57. Lv, T.; Peng, Y.; Zhang, G.; Jiang, S.; Yang, Z.; Yang, S.; Pang, H. How About Vanadium-Based Compounds as Cathode Materials for Aqueous Zinc Ion Batteries? *Adv. Sci.* **2023**, *10*, 2206907. [CrossRef]
58. Ding, Y.L.; Wen, Y.; Wu, C.; Van Aken, P.A.; Maier, J.; Yu, Y. 3D $V_6O_{13}$ Nanotextiles Assembled from Interconnected Nanogrooves as Cathode Materials for High-Energy Lithium Ion Batteries. *Nano Lett.* **2015**, *15*, 1388–1394. [CrossRef] [PubMed]
59. Xu, X.; Xiong, F.; Meng, J.; Wang, X.; Niu, C.; An, Q.; Mai, L. Vanadium-Based Nanomaterials: A Promising Family for Emerging Metal-Ion Batteries. *Adv. Funct. Mater.* **2020**, *30*, 1904398. [CrossRef]
60. Liu, Y.; Wu, X. Review of Vanadium-Based Electrode Materials for Rechargeable Aqueous Zinc Ion Batteries. *J. Energy Chem.* **2021**, *56*, 223–237. [CrossRef]
61. Yan, Y.; Li, B.; Guo, W.; Pang, H.; Xue, H. Vanadium Based Materials as Electrode Materials for High Performance Supercapacitors. *J. Power Sources* **2016**, *329*, 148–169. [CrossRef]
62. Rasoulis, M.; Vernardou, D. Electrodeposition of Vanadium Oxides at Room Temperature as Cathodes in Lithium-Ion Batteries. *Coatings* **2017**, *7*, 100. [CrossRef]
63. Pei, C.; Jin, M.; Yin, Y.; Xiong, F.; Jiang, Y.; Yuan, X.; Wang, F.; An, Q. Intercalation-Type $V_2O_3$ with Fast $Mg^{2+}$ Diffusion Kinetics for High-Capacity and Long-Life Mg-Ion Storage. *ACS Sustain. Chem. Eng.* **2020**, *8*, 16164–16171. [CrossRef]
64. Zuo, C.; Tang, W.; Lan, B.; Xiong, F.; Tang, H.; Dong, S.; Zhang, W.; Tang, C.; Li, J.; Ruan, Y.; et al. Unexpected Discovery of Magnesium-Vanadium Spinel Oxide Containing Extractable $Mg^{2+}$ as a High-Capacity Cathode Material for Magnesium Ion Batteries. *Chem. Eng. J.* **2021**, *405*, 127005. [CrossRef]